

# Achieving an Efficient and Stable Morphology in Organic Solar Cells Via Fine-Tuning the Side Chains of Small-Molecule Acceptors

Meijia Chang,<sup>1</sup> Lingxian Meng,<sup>1</sup> Yunchuang Wang, Xin Ke, Yuan-Qiu-Qiang Yi, Nan Zheng, Wenyu Zheng, Zengqi Xie, Mingtao Zhang, Yuanping Yi, Hongtao Zhang, Xiangjian Wan, Chenxi Li, and Yongsheng Chen\*

Cite This: *Chem. Mater.* 2020, 32, 2593–2604

Read Online

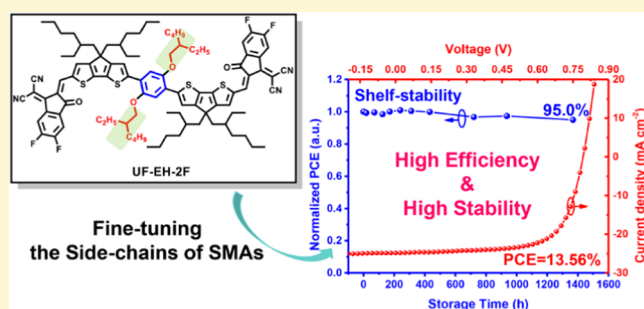
ACCESS |

Metrics & More

Article Recommendations

Supporting Information

**ABSTRACT:** Both the efficiency and stability of low-cost organic solar cells are central components for meeting the requirements of commercialization for organic photovoltaics (OPV). Furthermore, the relationship between the chemical structure of an active material and morphology and its effects on efficiency and stability is still largely undetermined. Additionally, both the kinetic and thermodynamic morphology states of an active layer can have a huge impact on efficiency and stability, even when the chemical structures of materials applied in the active layer are especially the same or similar. Here, using two series of acceptor–donor–acceptor (A–D–A)-type small-molecule acceptors (SMAs) with similar backbone structures, we demonstrate the relevance of fine-tuned chemical structures with their solution and solid-state properties, further leading to significantly different behavior in terms of both device efficiency and stability. This is also partially due to the different morphology states caused by such fine chemical structure tuning. Our results indicate that a delicate balance of molecular aggregation and ordered stacking morphology is required to achieve and lead to high efficiency and stability. Thus, among the two series of molecules, UF-EH-2F, with both optimal length and steric hindrance of side chains, achieves the preponderant morphology in its corresponding device, where its morphologies “efficient state” and “stable state” are almost overlapped, and thus lead to both the highest efficiency (power conversion efficiency, PCE = 13.56%) and the best stability. Our results indicate that it is highly possible to achieve the morphology state required for both high efficiency and stability simultaneously by fine-tuning the chemical structure of active materials for organic solar cells.



## INTRODUCTION

Both the efficiency and stability of low-cost organic solar cells are central components to meeting the requirements of commercialization for organic photovoltaics (OPV).<sup>1</sup> While significant developments with efficiencies up to 16–17% have been achieved,<sup>2–5</sup> materials and devices that possess both the desired efficiency and stability needed for commercial purposes are still unavailable. This may partially be due to the limited understanding of the relationship between the chemical structure of active layer materials and its corresponding morphology state. Furthermore, currently, in most cases, the optimized morphology state for high power conversion is far away from the thermodynamically stable state,<sup>6,7</sup> which leads to the morphology downgrading and an eventual decline in device performance.

It is well known that efficiency and stability depend on both the molecular- and morphology-level properties of the active materials in the active layers.<sup>8,9</sup> This is echoed by many results demonstrating that even with the same or similar chemical structures, and thus similar molecular levels and solution properties, device performance can be very different in terms of

both efficiency and stability.<sup>7,10–16</sup> Furthermore, the relationship between efficiency and stability is quite elusive in the literature. All these have been hammering to realize the goal of achieving highly efficient and stable OPV materials and devices to meet the requirements of commercial applications.<sup>1,17</sup>

In regard to stability, there are many complicated intrinsic and external factors in effect.<sup>18</sup> The external factors include water and oxygen from the atmosphere, which can be well prevented by proper and sophisticated encapsulation used in the industry.<sup>19</sup> Additionally, the intrinsic factors clearly depend on the chemical structures of the materials, particularly the ones in active layers. Considering that organic materials have been used in commercial organic light-emitting diodes (OLED), it is reasonable to assume that the intrinsic chemical

Received: January 10, 2020

Revised: March 4, 2020

Published: March 4, 2020

stability of active materials could be achieved in the future by following the same strategy as that applied for OLED materials.<sup>19</sup> The other side of intrinsic stability is morphology stability.<sup>20–24</sup> In the fabrication process of OPV devices, the formation of corresponding bulk–heterojunction morphologies comes down to the kinetic crystallization of donors and acceptors in a very short period. Therefore, it is natural at this stage to obtain an unstable/metastable morphology with improperly mixed domains and phase separation in the active layers.<sup>26</sup> It is also well known that the morphology of active layers can be carefully optimized to ensure an appropriate phase separation for efficient quantum conversion, which can simultaneously maximize the photon absorption, exciton separation, and charge transportation for a high power conversion efficiency (PCE) value in devices. However, even after such performance optimization, both the donor and acceptor molecules in the active layer might still migrate and rearrange into a thermodynamic equilibrium (or more stable) state during the path of long-time utilization.<sup>25–28</sup> In other words, even with optimized initial performance, its performance might still degrade over time.

In the following, with a given OPV material system (e.g., the active materials such as donor and acceptor materials are set for a BHJ-type device), we will use the term “kinetic state” to represent the initial metastable state of morphology obtained after the device-fabrication process. The term “efficient state” will be used to represent the ideal morphology state of such a material system, which should have the optimal phase separation and morphology and thus result in the possible highest (best intrinsic) PCE value of the corresponding devices. Lastly, the term “stable state” is applied to represent the thermodynamic equilibrium (most stable) state of morphology for the given material system.

With these considerations, we argue that, at least in theory, if a morphology state for a given OPV system, with the characteristics of both efficient and stable states, could be achieved at the initial stage of device fabrication (corresponding to the kinetic state), both high stability and efficiency of OPV devices could be achieved (as shown in Figure 1).<sup>29</sup> That

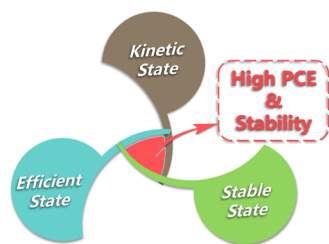


**Figure 1.** Schematic diagram of the relationship between kinetic state, efficient state, and stable state.

is, if the achieved initial state (kinetic state) during the device-fabrication process can be overlapped with both the efficient and stable states,<sup>30</sup> the device would be both highly efficient and stable.

From state-of-the-art studies in the literature,<sup>31–34</sup> it is clear that while we have many means to predict and control the molecular level and solution properties of active materials, such as designing the right molecules to have the desired electronic properties,<sup>35–39</sup> solubility,<sup>40</sup> film quality,<sup>41,42</sup> and so on, it is still quite elusive to control or predict their morphology state and solid-state properties, particularly for the complicated

interpenetrating mixed state of the donor and acceptor, as in the case of BHJ. This is the main challenge to be addressed during further studies, and the development of OPV for the eventual goal of its commercial application. In this regard, it is extremely important to link chemical structures with both their corresponding morphology state and device efficiency in the active layer, where the donor and acceptor molecules are mixed up to result in a rather complicated multiscale/level interpenetrating and heterogeneous morphology.<sup>43</sup> It would be ideal to predict and control the molecular-level property and morphology (solid properties with D/A together) at the beginning of molecule design, or at least have some ideas as to how to do so.

With these considerations, we designed three pairs in two series of six A–D–A-type small-molecule acceptors (SMAs) in this work, all with the same backbone and essentially similar molecular and solution properties, and investigated systematically the relationship between their fine-tuning chemical structures and morphology, including in pure and blend states. From there, a clear relationship has been obtained in regard to their chemical structure, performance, and stability. It is concluded that to achieve both efficient and stable active materials, their initial morphology state (kinetic state) needs to be the same as or close enough to both the efficient state (i.e., an optimal nanoscale interpenetrating state between D and A) and stable state in the active layer. Furthermore, our results indicate that one way to achieve such an overlapped morphology state is by fine-tuning the side chains of acceptors. Thus, among these two series of molecules, UF-EH-2F with both optimal length and steric hindrance of side chains exhibits the property to be able to achieve its efficient state and stable state with its kinetic state overlapped in the device-fabrication process, which offers both the highest PCE of 13.56% and the best stability (5% loss after 1368 h when stored in a glovebox without encapsulation) among all of these molecules. These results and conclusions are expected to offer some important guidelines for future molecule design with both high stability and efficiency.

## RESULTS AND DISCUSSION

**Molecular Design and Synthesis.** With the consideration of a simple synthesis route and low cost, two common and easily accessible building blocks 2,5-bis(alkoxy)benzene and 4,4-bis(2-ethylhexyl)-4*H*-cyclopenta[2,1-*b*:3,4-*b'*]-dithiophene (CPDT) were selected to construct the six targeted small acceptor molecules with an unfused architecture (Figure 2). Note that the backbone and end unit (2-(5,6-difluoro-3-oxo-2,3-dihydro-1*H*-inden-1-ylidene)malononitrile) in these molecules were chosen based on the literature, and the corresponding SMAs achieved good device performance,<sup>44–47</sup> where it is believed that these molecules would offer at least decent performance as the base to carry out our studies. Meanwhile, fine-tuning the side chains of these SMAs could ensure similar properties at the molecule level,<sup>48,49</sup> which offers the base to study the relevance between morphology state, efficiency, and device stability.

The first series of three molecules have methyl, isobutyl, and propyl as the substitutions on the central benzene ring, compared with the second series of the other three molecules, where the corresponding groups are all prolonged with octyl, *iso*-octyl, and 3-octyl groups, respectively (Figure 2), to address the solubility issue discussed below. Notably, all six of these

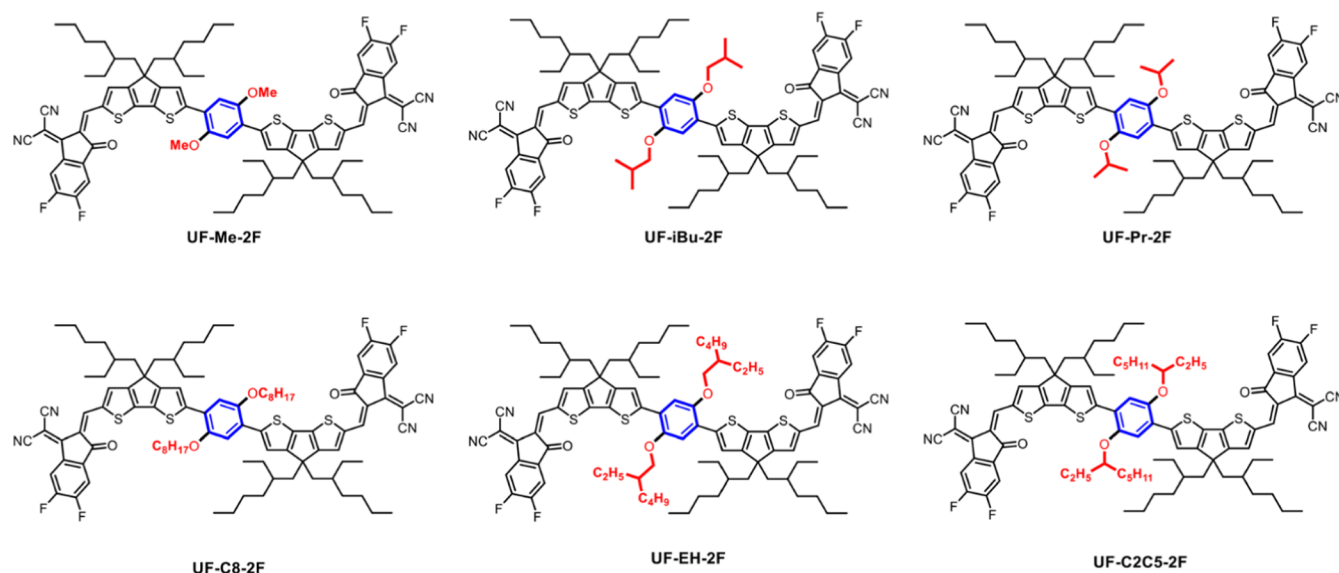


**Figure 2.** Chemical structures of the six unfused SMAs by adjusting the length and steric hindrance of side chains at the central benzene rings.

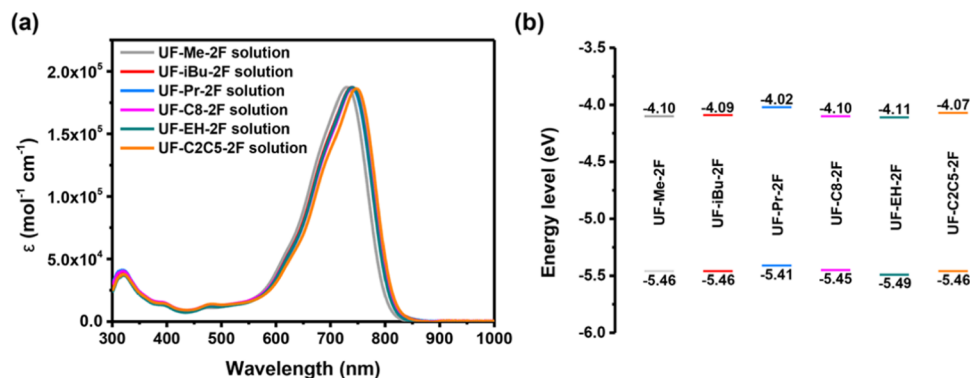


**Figure 3.** (a) Absorption spectra of all SMAs in chloroform with the same concentration ( $4.3 \times 10^{-6}$  mol L<sup>-1</sup>). (b) Energy levels of all SMAs measured by UPS. The HOMO values were calculated by the incident photon energy,  $h\nu = 21.22$  eV,  $E_{\text{cutoff}}$  and  $E_{\text{onset}}$ . The LUMO values were calculated with the  $E_{\text{g}}^{\text{opt}}$  and HOMO energy level.

molecules were synthesized in only three simple and high-yield steps (Figure S1 in the Supporting Information).

**Absorption and Electrochemical Properties.** The corresponding ultraviolet–visible–infrared (UV–vis–NIR) absorption spectra of these SMAs in a dilute chloroform solution are shown in Figure 3a. The maximum absorption wavelengths ( $\lambda_{\text{max}}$ ) of all SMAs are around 730–740 nm, and the solution extinction coefficients are all approximately  $1.87 \times 10^5$  mol<sup>-1</sup> cm<sup>-1</sup>. Clearly, all these six SMAs exhibit similar light absorption in terms of patterns and intensities. A similar conclusion was obtained from their electrochemical studies. The energy levels of all SMAs show little difference, measured by cyclic voltammetry in a dichloromethane (CH<sub>2</sub>Cl<sub>2</sub>) solution (Figure S4 and Table S9), consistent with the calculation results of the highest occupied molecular orbital (HOMO)/lowest unoccupied molecular orbital (LUMO). However, their solid-state electrochemical properties, shown in Figure 3b and determined by ultraviolet photoelectron spectroscopy (UPS) measurements (Figure S5), show slight differences in energy levels. These results indicate that, as expected, the fine-tuning of side chains with different lengths and steric hindrances of these SMAs has some impact on their molecular packing even in a pure solid state.

**Photovoltaic Performance.** With similar absorption properties in the dilute solution of all SMAs, J52 (the molecular structure is illustrated in Figure 4a) was selected as the donor material to investigate its photovoltaic properties and device stability due to its matched HOMO/LUMO and also complementary absorption. The OPV devices were fabricated with an inverted structure (indium-tin oxide, ITO/ZnO/PFN-Br/active layer/MoO<sub>x</sub>/Ag), and the photovoltaic properties of all SMAs were fully investigated under various process conditions/parameters (detailed in Tables S2–S7). The optimized photovoltaic results of all devices based on J52:SMAs are summarized in Table 1. Importantly, two series of SMAs revealed the same tendency: the SMAs with moderate steric hindrance of side chains (UF-iBu-2F and UF-EH-2F) displayed the best device performance among each series. However, the three SMAs with short side chains have overall lower performance compared to the corresponding SMAs with prolonged side chains, mainly due to the solubility issue. Note that, among all these six SMAs, the UF-EH-2F-based device exhibited the best PCE of 13.56%, with a  $V_{\text{oc}}$  of 0.79 V, an outstanding  $J_{\text{sc}}$  of 24.87 mA cm<sup>-2</sup>, and a significantly enhanced fill-factor (FF) of 0.69. To the best of our knowledge, this is also the highest PCE value of OPV devices based on unfused SMAs.<sup>44,46,50</sup> According to the external quantum efficiency

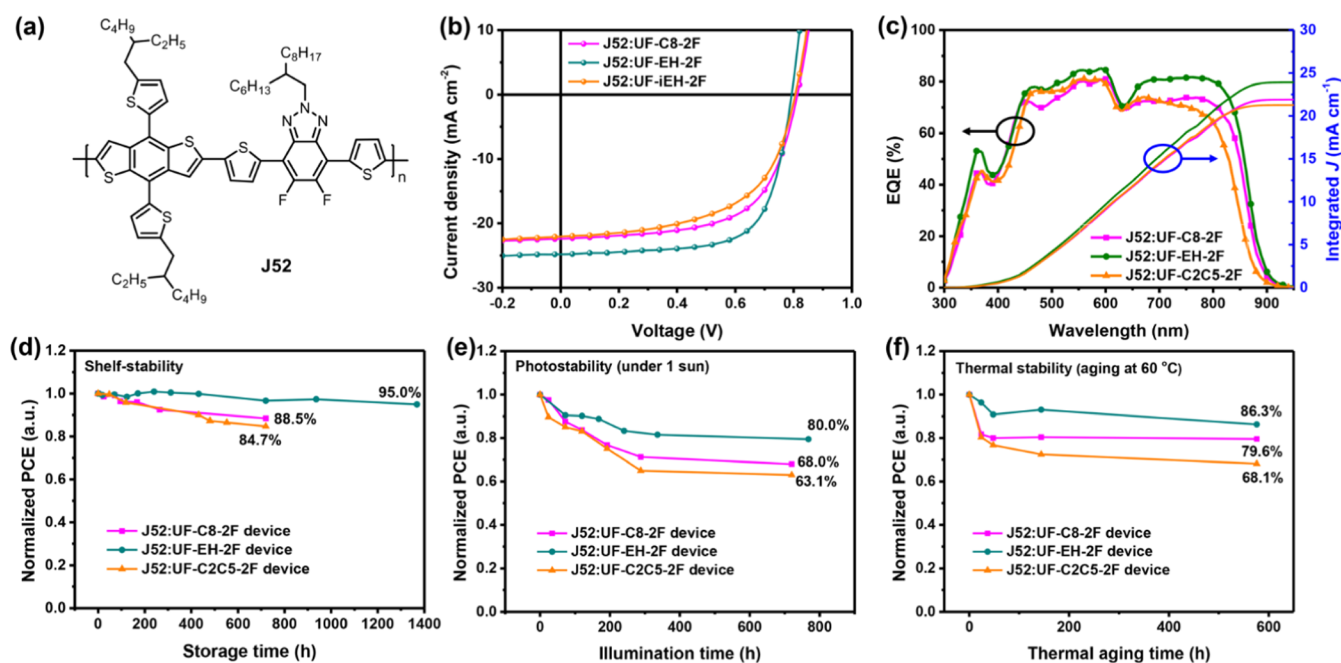


**Figure 4.** (a) Chemical structure of the polymer donor J52. (b)  $J$ - $V$  and (c) EQE curves of the optimized devices based on J52:UF-C8-2F, J52:UF-EH-2F, and J52:UF-C2C5-2F under the illumination of AM 1.5G, 100 mW cm<sup>-2</sup>. (d) Shelf stability, (e) photostability, and (f) thermal stability of the devices based on J52:UF-C8-2F, J52:UF-EH-2F, and J52:UF-C2C5-2F.

**Table 1. Photovoltaic Parameters of the Optimized J52:SMAs-Based Devices Under the Illumination of AM 1.5G, 100 mW cm<sup>-2</sup>**

active layer <sup>a</sup>	$V_{oc}$ (V)	$J_{sc}$ (mA cm <sup>-2</sup> )	FF	PCE <sup>b</sup> (%)	$J_{sc,EQE}$ <sup>c</sup> (mA cm <sup>-2</sup> )
J52:UF-Me-2F	0.82 (0.81 ± 0.01)	14.03 (13.89 ± 0.16)	0.50 (0.49 ± 0.01)	5.75 (5.62 ± 0.14)	
J52:UF-C8-2F	0.81 (0.81 ± 0.01)	22.39 (22.33 ± 0.46)	0.62 (0.61 ± 0.01)	11.24 (11.15 ± 0.24)	22.23
J52:UF-iBu-2F	0.79 (0.79 ± 0.01)	21.95 (21.66 ± 0.18)	0.62 (0.62 ± 0.01)	10.75 (10.32 ± 0.28)	
J52:UF-EH-2F	0.79 (0.79 ± 0.01)	24.87 (24.49 ± 0.34)	0.69 (0.69 ± 0.01)	13.56 (13.31 ± 0.19)	24.26
J52:UF-Pr-2F	0.80 (0.80 ± 0.01)	21.58 (21.35 ± 0.13)	0.54 (0.53 ± 0.01)	9.32 (8.99 ± 0.21)	
J52:UF-C2C5-2F	0.80 (0.81 ± 0.01)	22.05 (21.94 ± 0.25)	0.57 (0.56 ± 0.01)	10.05 (9.87 ± 0.26)	21.20

<sup>a</sup>The optimized active layers had a donor/acceptor weight ratio of 1:1.2, spin-coated from a solvent mixture of chloroform with 0.5% 1-chloronaphthalene (CN) in volume, and further annealed at 120 °C for 10 min before electrode deposition. <sup>b</sup>The average PCE values with standard deviations were obtained from 20 devices. <sup>c</sup>The values are calculated from the corresponding EQE spectra.

(EQE) spectra in Figure 4c, all devices have the photovoltaic responses in the broad range of 450–900 nm, owing to the complementary absorptions of the donor and acceptor. The calculated  $J_{sc}$  values from EQE curves are all close to the measured values from  $J$ - $V$  curves within a 4% mismatch. Notably, the different  $J_{sc}$  values of devices based on these SMAs were mainly caused by the photoresponse in the range of 650–900 nm (contributed mainly by the SMAs). The EQE value in the contribution part of the acceptor was around 80% of the UF-EH-2F device, which is remarkably higher than that of UF-C8-2F and UF-C2C5-2F and consistent with its higher  $J_{sc}$  value of the device.

**Device Stability.** To evaluate the stability of devices, we measured the shelf stability, photostability, and thermal stability of the devices based on these SMAs. Figure 4d–f shows the photovoltaic performance of the devices as a function of storage time, where the unencapsulated devices were placed in an argon-filled glovebox. The UF-EH-2F-based devices exhibited the best shelf stability (Figure 4d), with only 3.3% loss of the initial PCE after 30 days (720 h), which outperformed those based on UF-C8-2F (11.5% loss after 30 days) and UF-C2C5-2F (15.3% loss after 30 days). Even after

57 days (1368 h), the UF-EH-2F-based devices could also maintain 95.0% of their initial performance. Photostability (Figure 4e) was also tested under a continuous white light-emitting diode (LED) illumination (1 sun) in a glovebox, and the UF-EH-2F-based devices demonstrated the best stability (80.0% of their initial performance after 32 days), significantly better than that of UF-C8-2F (68.0% of the initial PCE after 30 days) and UF-C2C5-2F (63.1% of the initial PCE after 30 days). Thermal stability (Figure 4f) of these devices gave the same conclusion, which indicates that the UF-EH-2F-based device has the best stability. More details of the photovoltaic parameters ( $V_{oc}$ ,  $J_{sc}$ , and FF) as a function of time for the devices are plotted in the Supporting Information (Figure S6), consistent with the results above.

From the results discussed above, among all of these molecules, the devices based on UF-EH-2F showed not only the highest power conversion efficiency but also the best shelf stability, photostability, and thermal stability, though all SMAs possessed very similar molecular-level properties. Note that this coincident phenomenon for UF-EH-2F has not been widely observed as far as we know, and thus, prompted us to take up further studies and understand the reasons behind.

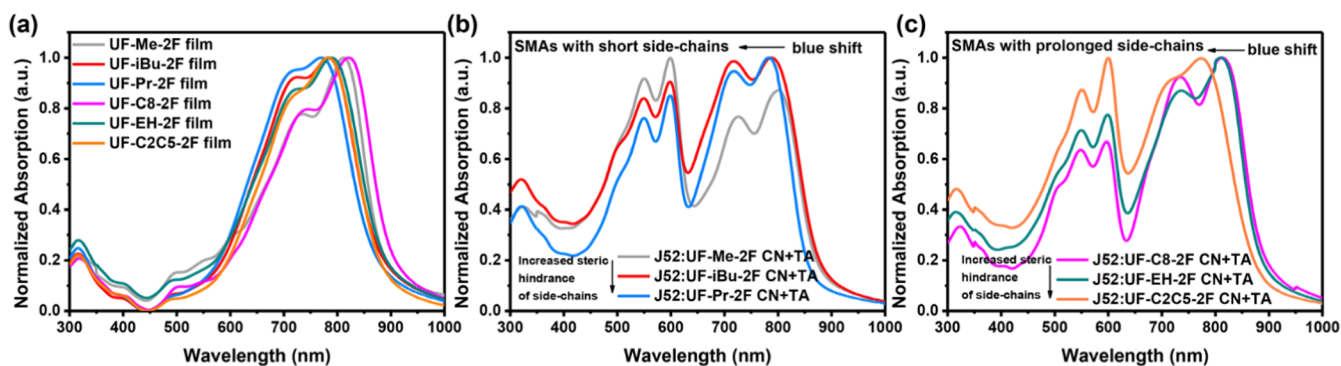


**Figure 5.** (a) Normalized absorption spectra of all SMAs in the solid film state prepared by spin-coating from a  $\text{CHCl}_3$  solution. Absorption spectra of optimized (b) J52:UF-Me-2F/UF-iBu-2F/UF-Pr-2F blend films and (c) J52:UF-C8-2F/UF-EH-2F/UF-C2C5-2F blend films.

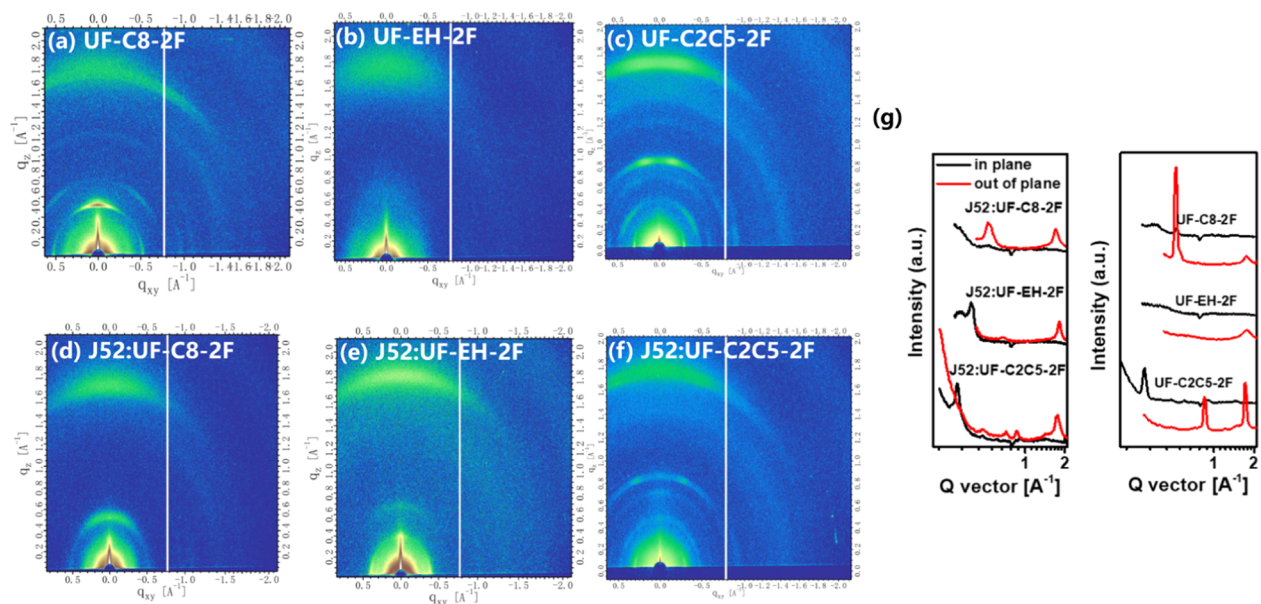


**Figure 6.** Two-dimensional (2D) GIWAXS patterns of the pure films (a) UF-C8-2F, (b) UF-EH-2F, and (c) UF-C2C5-2F, as well as the corresponding optimal blend films (d) J52:UF-C8-2F, (e) J52:UF-EH-2F, and (f) J52:UF-C2C5-2F. (g) Line-cut profiles of the corresponding GIWAXS patterns.

This led us to the following systematic investigation about the kinetic state, efficient state, and stable state of these molecules in BHJ OPV devices.

**Kinetic State vs Efficient State. Optical Absorption vs Efficiency.** Unlike similar absorption in solution (as shown in Figure 3a), the solid absorption spectra of all SMAs in the pure film state exhibit significant differences (Figure 5a). The  $\lambda_{\text{max}}$  values of these SMAs in the pure film state display clear blue shifts with the increased steric hindrance of side chains (from UF-Me-2F to UF-Pr-2F and UF-C8-2F to UF-C2C5-2F), consistent with the packing density results of atomistic molecular dynamics simulations (shown in the Supporting Information). Furthermore, all the SMAs with prolonged side chains exhibit a red-shifted absorption in contrast to the counterpart molecules with shorter side chains (UF-Me-2F vs UF-C8-2F, UF-iBu-2F vs UF-EH-2F, and UF-Pr-2F vs UF-C2C5-2F), probably due to the increased side-chain interaction from the prolonged side chains.<sup>41</sup> The slightly different optical band gap ( $E_{\text{g}}^{\text{opt}}$ ) of each SMAs was calculated from its absorption onset and the corresponding data are summarized in Table S10.

For blend films with J52 (Figure 5b,c) obtained during the device optimal fabrication, the absorption spectra change was the same as that of the pure films. With the increased steric hindrance of side chains in each series, the UV–vis–NIR absorption spectra under the optimal conditions were slightly blue-shifted. Furthermore, the absorption spectra of the blend films based on the SMAs with prolonged side chains (but with similar steric hindrance) showed a red shift compared to the corresponding short ones (such as the pair of UF-Me-2F vs UF-C8-2F). However, compared with their corresponding pure films, only the blend films of UF-iBu-2F and UF-EH-2F with moderate steric hindrance of side chains showed significant red shifts, and all the other four SMAs were slightly blue-shifted (Figure S7). These results indicated that the packing properties of SMAs in blend films were changed more significantly compared with those in the pure film state by a minor change in the side chains on the benzene ring. Additionally, a more delicate balance in terms of both side-chain length and steric hindrance, as in the case of UF-EH-2F, seems to be achieved for the most optimal absorption in the active layer. Furthermore, as shown in Figure 3e, the EQE data of their corresponding devices are consistent with these

absorption results in Figure 5c, where the UF-EH-2F-based device exhibits both the widest and highest (which will be discussed below) photoresponse. This is consistent with the highest  $J_{sc}$  for the UF-EH-2F device (Table 1), contributing to its highest PCE among all six compounds.

**Morphology vs Efficiency.** The remarkable difference in absorption from solution to a pure state and a further blend state indicates that the packing and morphology of these molecules in the solid state must be different due to the fine-tuning of the chemical structures caused by the side chains on the benzene ring. More detailed investigations of morphologies were carried out on the series of SMAs with prolonged side chains (UF-C8-2F, UF-EH-2F, and UF-C2C5-2F) due to their overall higher performance.

First, as displayed in the atom force microscopy (AFM) height images (Figure S8), while all blend films displayed a very uniform and smooth surface with small root-mean-square roughness (1.33, 1.43, and 1.26 nm for UF-C8-2F, UF-EH-2F, and UF-C2C5-2F blend films, respectively), the UF-EH-2F-based blend film featured grain-like domains and exhibited a more defined phase separation compared with the others. Furthermore, compared with the UF-C8-2F and UF-C2C5-2F blend films, the UF-EH-2F blend film shows more continuous nanofiber-like networks in transmission electron microscopy (TEM) images (Figure S9). The optimal morphology for the UF-EH-2F blend film was also supported by the two-dimensional grazing-incidence wide-angle X-ray scattering (2D-GIWAXS) studies on their corresponding pure and blend films (Figure 6).

As can be seen from Figure 6a–c, all SMA neat films displayed (100) lamellar pecking peaks in the in-plane (IP) direction and pronounced (010)  $\pi$ – $\pi$  stacking peaks in the out-of-plane direction, indicating that all neat films showed ordered packing with a favored face-on orientation. Note that the slightly different positions of the (010) diffraction peaks of UF-C8-2F, UF-EH-2F, and UF-C2C5-2F, located in 1.75, 1.75, and 1.71  $\text{\AA}^{-1}$ , respectively, indicate their slightly different  $\pi$ – $\pi$  stacking distances of 3.58, 3.58, and 3.66  $\text{\AA}$ .

After blending with a donor, the blend films under the optimized conditions also displayed a broad and combined diffraction peak in their (010) regions along the OOP direction, indicative of the same face-on orientation for the donor and all acceptor molecules (Figure 6d–f). However, their  $\pi$ – $\pi$  stacking distances of the blend films are significantly different. The optimized UF-EH-2F blend film shows a  $\pi$ – $\pi$  stacking peak at 1.80  $\text{\AA}^{-1}$ , corresponding to a distance of 3.49  $\text{\AA}$ , which is much smaller than that of the UF-C8-2F (3.67  $\text{\AA}$ ) and J52:UF-C2C5-2F (3.58  $\text{\AA}$ ) blend films. Moreover, the UF-EH-2F blend film also displays a larger crystal coherence length (CCL) of 47.50  $\text{\AA}$ , estimated using the Scherrer equation, than that of the UF-C8-2F (35.20  $\text{\AA}$ ) and UF-C2C5-2F (38.03  $\text{\AA}$ ) blend films. The smaller  $\pi$ – $\pi$  stacking distance and the increased CCL of the UF-EH-2F blend film indicate that the UF-EH-2F blend film formed an enhanced and better-ordered packing and higher crystallinity, which is beneficial for charge transport in OPV devices.<sup>51</sup>

To investigate the miscibility between J52 and SMAs, we measured the contact angle and calculated their surface tensions for all pristine materials and the interfacial tensions for the corresponding blend films (Figure S10 and Table S11) following the literature method.<sup>52</sup> According to the contact angle, the UF-EH-2F pure film exhibits lower surface tension than that of UF-C8-2F and UF-C2C5-2F. Then, the equation

$\chi \propto (\sqrt{\gamma_{\text{donor}}} - \sqrt{\gamma_{\text{acceptor}}})^2$ , suggested by Moons and co-workers in which  $\chi$  is the Flory–Huggins interaction parameter of two blends, was used to further compare the miscibility of the blend films.<sup>53</sup> The  $\chi$  parameter of the J52:UF-EH-2F blend film is higher than that of the UF-C8-2F and UF-C2C5-2F blend films, indicating lower miscibility and the potential for higher domain purity in the UF-EH-2F-based device.

All of these results indicate that the UF-EH-2F blend film exhibits a morphology state with optimal ordered packing properties and better domain purity by its proper fine-tuning of side chains among the six acceptors. Thus, its initial morphology state (kinetic state) achieved during the device fabrication for this molecule is also favorable for efficient photocurrent conversion, that is, its kinetic state is overlapped with or close to the desired efficient state, resulting in the best performance among these molecules.

**Comparison of Charge Generation, Transport, and Recombination.** Such a phenomenon of overlapping of the kinetic state with the efficient state for UF-EH-2F and the morphological differences of these SMAs are also supported by studies of charge separation, transport, and recombination in the devices. Initially, we examined the photocurrent density  $J_{ph}$  ( $J_{ph} = J_L - J_D$ ) as a function of the effective voltage  $V_{\text{eff}}$  ( $V_{\text{eff}} = V_0 - V_a$ ) of the devices to illustrate the exciton dissociation and charge-collection behavior. The charge dissociation probability ( $P_{\text{diss}}$ ) was estimated from the ratio of  $J_{ph}/J_{\text{sat}}$  under the short circuit and maximal power output conditions. As shown in Figure S11a, the devices based on UF-EH-2F showed  $P_{\text{diss}}$  values of 95.2 and 82.8% under the short circuit and maximal power output conditions, respectively, both higher than those of UF-C8-2F (92.2/72.8%) and UF-C2C5-2F (93.2/68.2%). The light intensity ( $P_{\text{light}}$ ) dependence of the  $J_{sc}$  and  $V_{oc}$  was tested to further understand the charge recombination kinetics of the devices. From Figure S11b, the  $\alpha$  value of the UF-EH-2F-based device was closer to 1, which indicates that the UF-EH-2F-based device has the weakest bimolecular recombination. The slope of  $V_{oc}$  vs  $P_{\text{light}}$  was used to determine the degree of trap-assisted recombination in the devices. From the  $V_{oc}$ – $P_{\text{light}}$  plot (Figure S11c), the devices based on UF-EH-2F showed a slope of 1.055kT/q, which is much closer to kT/q than that of both UF-C8-2F (1.233 kT/q) and UF-C2C5-2F (1.245 kT/q). Meanwhile, as depicted in the internal quantum efficiency (IQE) curves (Figure S11d), the UF-EH-2F device shows an IQE value of nearly 90% in the 650–850 nm region, which is much higher than that of UF-C8-2F- and UF-C2C5-2F-based devices. These results are consistent with the morphology analysis above and indicate that among all molecules, UF-EH-2F-based devices achieve not only a higher exciton dissociation rate and charge-collection efficiency but also lower trap density and weaker trap-assistant recombination. This results in the high  $J_{sc}$  and enhanced FF among all these OPV devices,<sup>12</sup> indicating that it indeed has also achieved a morphology state that is overlapped with or close to the desired efficient state during the device fabrication.

The transient photovoltage and photocurrent (TPV and TPC) were also measured to further understand the charge recombination dynamics of the devices. The results (as shown in Figure S12) show that UF-EH-2F-based devices have a relatively longer carrier lifetime (TPV, Figure S12a) and a much shorter charge sweepout time (TPC, Figure S12b), which is correlated to a weaker recombination and the observed higher electron mobility in the UF-EH-2F-based

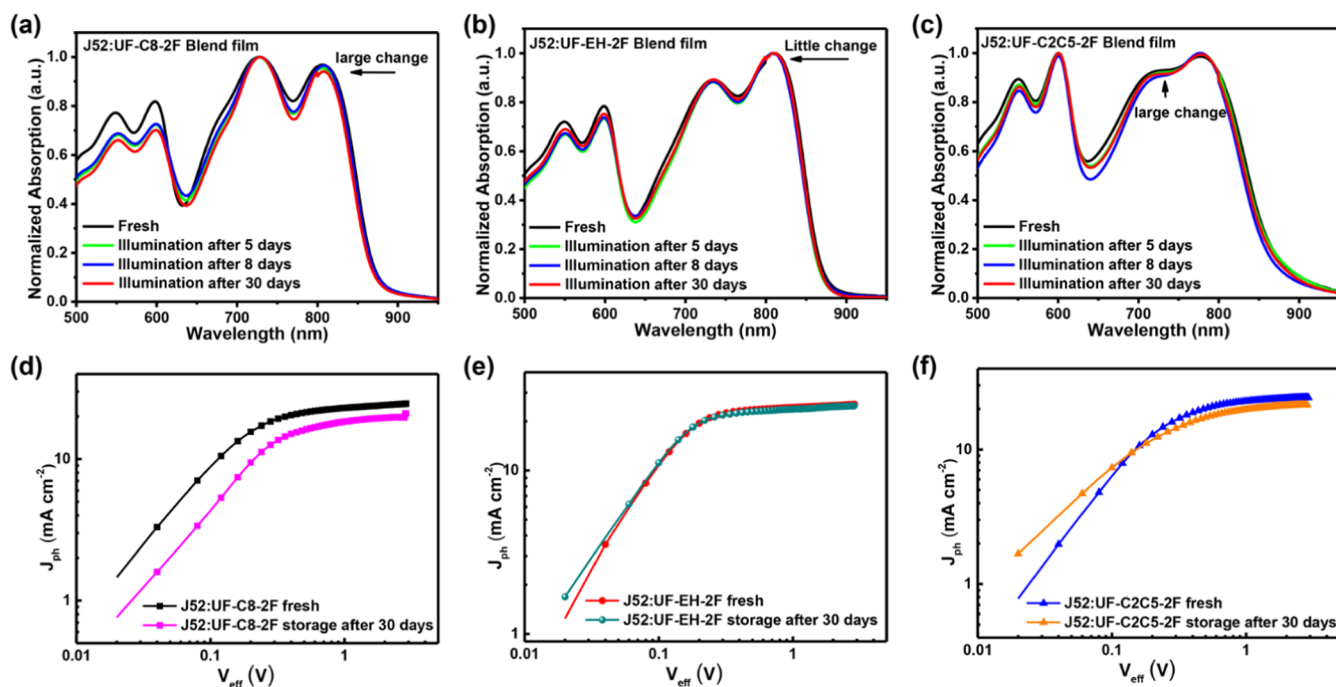


**Figure 7.** Absorption spectra changes of optimized (a) J52:UF-C8-2F, (b) J52:UF-EH-2F, and (c) J52:UF-C2C5-2F blend films under continuous white LED illumination (1 sun). The blend films were prepared by spin-coating from a CHCl<sub>3</sub> solution under optimized conditions.  $J_{ph}$  versus  $V_{eff}$  curves of the fresh and aged (d) J52:UF-C8-2F, (e) J52:UF-EH-2F, and (f) J52:UF-C2C5-2F devices stored in a glovebox.

devices (detailed in the Supporting Information, Table S8).<sup>54</sup> Furthermore, the hole and electron mobilities of the devices based on UF-EH-2F were more balanced than those of UF-C8-2F and UF-C2C5-2F (Table S8). Photoluminescence (PL) quenching experiments were also carried out to confirm the charge-transfer behavior in the blend films (Figure S13). When excited at 780 nm, the PL spectrum was more effectively quenched (nearly 90%) in the UF-EH-2F blend film than that of UF-C8-2F and UF-C2C5-2F. These results suggest that the UF-EH-2F blend film showed a more effective charge transfer.

All these results indicate that the UF-EH-2F device achieved the most suitable/optimal morphology state for efficient power conversion (corresponding to the efficient state) among these SMAs from the device-fabrication process, that is, the kinetic state obtained during its device fabrication is very likely to overlap with or be at least close to its efficient state. It should be pointed out that while in theory, it is possible that this achieved efficient state of UF-EH-2F may actually not be exactly the ideal morphology for its possibly highest OPV performance, we argue that the state achieved should be at least close to the state for the highest possible performance state. This is based on the following two reasons: (1) the total of six very similar molecules and the large number of tests performed under different processing parameters, solvents, etc. for each molecule should allow for a wide range of coverage to obtain many different morphology states, which should very likely include the one for the highest possible OPV performance, and (2) the obtained optimal results for UF-EH-2F, such as those of high FF (close to 70%) and EQE (close to 80%) and those from the photodynamic studies above, indicate that its high OPV performance should come from an optimal morphology state (otherwise, these parameters should not be that high).

**Kinetic State vs Stable State.** As we all know, the achieved initial morphology state (kinetic state) during the

device-fabrication process and the state for optimal power conversion (efficient state) may not be a thermodynamically stable morphology state (stable state).<sup>24,55</sup> This would lead the morphology state in the fabricated device to migrate away from the initial kinetic state and efficient state, even if the kinetic state and efficient state have already overlapped as in the case of UF-EH-2F. Thus, this would result in unstable device performance.<sup>29</sup> That is, to achieve both an efficient and a stable device, all three states, kinetic state, efficient state, and stable state, should be the same or close enough.<sup>29</sup> As discussed in the last section for the performance among all of the molecules, the UF-EH-2F-based device achieved a morphology state that exhibits the characteristics of a rather efficient state. This demonstrates that by fine-tuning the chemical structure, such as with appropriate length and steric hindrance of side chains, it is possible to render the initial morphology state (kinetic state) close to the efficient state of the active layer. Now, we need to understand whether and how the kinetic state is also overlapped with the stable state proposed at the beginning.

First, based on the stability test results discussed above, it is fair to conclude that UF-EH-2F has achieved the desired stable state or at least both states should be very close for the case of UF-EH-2F, since its device performance exhibits rather high stability and also the best stability among all of the devices of the designed acceptor molecules after numerous device optimizations. In other words, the kinetic state for the UF-EH-2F blend film is also overlapped with or close to the stable state. This conclusion is supported further below with detailed photophysical and morphology studies.

To find out whether UF-EH-2F has achieved the stable state directly, first, the UV-vis-NIR absorption spectra changes vs time with continuous heating at 60 °C for the blend films prepared under the same conditions as those of the optimal device fabrication were measured. As shown in Figure S14, the

absorption of the UF-EH-2F blend film does not change after heating for 72 h. Furthermore, Figure 7a–c shows the results of a similar test but with even harsher conditions, where the absorption vs time study was carried out under continuous white LED illumination (1 sun) in a glovebox for 30 days. Compared with the initial films, the absorption of the aged UF-EH-2F blend film exhibits only a very minor change (Figure 7b). These results indicate that the morphology state obtained during the device-fabrication process is quite stable for UF-EH-2F.

The morphological changes of the UF-EH-2F-based blend film were further directly monitored using GIWAXS during aging, and the summary of the parameters for the corresponding blend films obtained from GIWAXS is displayed in Table 2. The patterns of fresh and aged blend films (both

**Table 2. Summary of the Parameters for the Fresh and Aged Blend Films Obtained from the GIWAXS**

active layer		$\pi$ - $\pi$ stacking (010)		
		$d_x$ (Å) <sup>a</sup>	FWHM (Å <sup>-1</sup> ) <sup>b</sup>	CCL (Å) <sup>c</sup>
J52:UF-C8-2F	fresh	3.67	0.161	35.20
	photo aged	3.70	0.156	36.26
	thermal aged	3.70	0.142	39.85
J52:UF-EH-2F	fresh	3.49	0.119	47.50
	photo aged	3.51	0.119	47.68
	thermal aged	3.51	0.118	48.02
J52:UF-C2C5-2F	fresh	3.58	0.149	38.03
	photo aged	3.56	0.141	40.09
	thermal aged	3.52	0.122	46.45

<sup>a</sup>The (010) diffraction peak along the  $q_z$ -axis. <sup>b</sup>Full width at half-maximum (FWHM) for the (010) peak along the  $q_z$ -axis. <sup>c</sup>Coherence length estimated from Scherrer's equation ( $CCL = 2\pi k/\text{FWHM}$ ) for the  $\pi$ - $\pi$  stacking of the face-on crystallite.

illumination and thermal aging) are shown in Figure S15. It is clearly shown that the UF-EH-2F-based blend film exhibits no obvious change in both IP and OOP directions, with almost no change for both the  $\pi$ - $\pi$  stacking distance and CCL. These results demonstrate directly and clearly that a stable state was achieved during the device fabrication for the UF-EH-2F-based device,<sup>20</sup> or its kinetic state has overlapped with its stable state. On the contrary, the cases of the other two SMAs (UF-C8-2F and UF-C2C5-2F) are very different, where there are significant changes in both their absorption spectra (Figure 7a,c) and GIWAXS patterns (Figures S15 and S16), indicating that there is some morphology rearrangement occurring in the blend films from their kinetic state toward their stable state. The change in the  $\pi$ - $\pi$  stacking distance and increased values of CCL for the cases of UF-C8-2F and UF-C2C5-2F, a good and direct indicator for the morphology/phase change (instability) in the active layer,<sup>56</sup> agree with their device stability testing results as discussed above, indicating that these two molecules certainly have not achieved a stable state during their device fabrication. In other words, their kinetic state is not overlapped with or close to their corresponding stable state, thus leading to their device downgrading during the stability test.

Such conclusions were further supported by the results of the charge-generation and charge-transport studies (Figure 7d–f). For the devices stored in the glovebox for 30 days, the aged UF-EH-2F-based device shows almost no change, with  $P_{\text{diss}}$  values of 95.0/81.5% (vs the initial values of 95.2/82.8%)

under the short circuit and maximal power output conditions, indicating that efficient charge dissociation and high charge-collection efficiency remain unchanged in the aged UF-EH-2F device (Figure 7e). However, for the other two SMAs (UF-C8-2F and UF-C2C5-2F), the  $P_{\text{diss}}$  values decreased significantly from 92.2/72.2 to 86.1/63.0% for the UF-C8-2F device (Figure 7d) and from 93.2/68.2 to 82.3/63.1% for the UF-C2C5-2F-based device (Figure 7f), respectively. From these results, it can be concluded that the initial morphology state (kinetic state) achieved during the device-fabrication process in the UF-EH-2F-based device is the same as or close enough to its thermodynamically stable state (stable state), leading to the hardly changed charge generation and transport.<sup>22</sup>

To sum up this section, for UF-EH-2F among all six molecules, its kinetic state, which has been proven to be rather close to or overlapped with the efficient state in the previous section, is also close to or overlapped with its thermodynamically stable state (stable state). This results in the corresponding devices with high efficiency and stability. This overlap of the three states for UF-EH-2F must come with its defined side chain since this is the only difference among all of the molecules. The *iso*-octyl of UF-EH-2F can ensure good solubility and also control the packing property and miscibility between a donor and an acceptor. The morphology state of UF-EH-2F displayed ordered molecular packing properties and enhanced intermolecular interactions, which are not only favorable for charge transport in the corresponding devices (resulting in the high  $J_{\text{sc}}$  and FF, efficient state) but also freeze the optimal morphology by inhibiting the diffusion of adjacent molecules and provide effective ways to achieve better stability (stable state). This indicates that proper tuning/engineering of molecular structures could offer both a stable and efficient state, the eventual goal of OPV molecule design.

To investigate the general applicability of our strategy and the concept of the three states, another well-known polymer donor PBDB-T was also used to fabricate OPV devices and performance studies were carried out in the same way. The device based on PBDB-T:UF-EH-2F exhibited the best performance, with a PCE of 12.60% among all acceptors (Table S12). The stability of the devices was also measured. Interestingly, the devices based on PBDB-T:UF-EH-2F also displayed high shelf stability (98.3% of the initial PCE after 120 h), photostability (88.5% of the initial PCE after 120 h), and thermal stability (75.5% of the initial PCE after 120 h), which is much better than that of UF-C8-2F- and UF-C2C5-2F-based devices (Figure S17). These results indicate that its kinetic state is also close to or overlapped with both the efficient state and stable state simultaneously in the PBDB-T:UF-EH-2F blend film. While further cases are needed, the same conclusion observed for these two donor molecules with our two series of six acceptor molecules indicates that there might be some general applicability of the three-state concept and the effectiveness of side-chain tuning with the same backbone.

## CONCLUSIONS

In summary, we have successfully demonstrated a clear relationship between both device performance and stability with chemical structures of active materials using a series of A–D–A-type acceptor molecules with the same backbone. Among the six molecules studied, the A–D–A SMA UF-EH-2F with suitable length and steric hindrance of side chains has achieved both the best performance with a PCE of 13.56% and

best stability, which is due to the overlap of its kinetic, efficient, and stable states. These results indicate that it is highly possible to achieve both high stability and efficiency by fine-tuning the side chains of acceptor molecules in the active layer molecules, assuming these molecules already have a decent backbone structure. This is believed to be achieved by having the initial morphology state (kinetic state) obtained during the device fabrication to be overlapped with or close enough to both the thermodynamically stable state (stable state) and the state of ideal morphology (efficient state). Note that the defined structure of small molecules designed for OPV would offer a strong advantage to apply this strategy to obtain such molecules with both efficient and stable OPV performance since the structure–efficiency–stability studies would offer more refined results. Considering the rich and widely available data in the literature for OPV, it is strongly believed that applying the same strategy of fine-tuning chemical structures on other reported high-performance molecules should be highly possible to realize the goal for both high performance and stability for truly commercial applications of OPV.

## EXPERIMENTAL SECTION

**Synthesis Method.** UF-C8-2F was selected as an example to illustrate the synthesis steps of SMAs, and the synthesis route is displayed in the Supporting Information (Figure S1).

**Synthesis of Compound 3.** A solution of compound 1 (1 g, 2.03 mmol) and compound 2 (3.37 g, 4.87 mmol) in dry toluene was degassed three times, followed by the addition of Pd(PPh<sub>3</sub>)<sub>4</sub> (23.5 mg, 0.020 mmol) as a catalyst. After stirring and refluxing under the protection of argon for 24 h, the mixture was extracted with CHCl<sub>3</sub> (50 mL × 3). The organic layer was combined and washed with water and dried with anhydrous Na<sub>2</sub>SO<sub>4</sub>. After removal of the solvent, the crude product was purified by a silica gel using dichloromethane and petroleum as eluents to give compound 3 as a yellow oil (1.18 g, 51% yield). Mass spectroscopy (MS) (matrix-assisted laser desorption/ionization-time of flight, MALDI-TOF): calcd for C<sub>72</sub>H<sub>110</sub>O<sub>2</sub>S<sub>4</sub> [M<sup>+</sup>] 1134.7389, found 1134.5147.

**Synthesis of Compound 4.** A Vilsmeier reagent, which was prepared with POCl<sub>3</sub> (2 mL, 21.5 mmol) in dry dimethylformamide (DMF) (8 mL), was added to a solution of compound 3 (400 mg, 0.35 mmol) in 1,2-dichloroethane (100 mL) at 0 °C and then stirred at room temperature for 2 h. After being stirred at 75 °C for 12 h, the mixture was poured into ice water (200 mL), neutralized with NaOAc, and then extracted with dichloromethane. The combined organic layer was washed with water and brine and dried over Na<sub>2</sub>SO<sub>4</sub>. After removal of the solvent, the crude product was purified by a silica gel using a mixture of dichloromethane and petroleum ether as an eluent to afford compound 4 as a red solid (352 mg, 84% yield). MS (MALDI-TOF): calcd for C<sub>74</sub>H<sub>110</sub>O<sub>4</sub>S<sub>4</sub> [M<sup>+</sup>] 1190.7287, found 1190.3589.

**Synthesis of Compound 5.** Compound 4 (100 mg, 0.084 mmol) and 2-(5,6-difluoro-3-oxo-2,3-dihydro-1H-inden-1-ylidene)-malononitrile (2F, 154.6 mg, 0.672 mmol) were dissolved in CHCl<sub>3</sub> (30 mL) and pyridine (0.7 mL) was added dropwise. Under the protection of argon, the mixture was stirred overnight at room temperature. After removal of the solvent, the crude product was purified by a silica gel using chloroform as an eluent to afford the target material compound 5 (UF-C8-2F) as a dark blue solid (104.5 mg, 77% yield). <sup>1</sup>H NMR (400 MHz, CDCl<sub>3</sub>) δ 8.90 (s, 2H), 8.52 (dd, *J* = 10.0, 6.6 Hz, 2H), 7.65 (t, *J* = 7.5 Hz, 4H), 7.54 (s, 2H), 7.30 (s, 2H), 4.21 (t, *J* = 6.0 Hz, 4H), 2.08–1.95 (m, 12H), 1.66–1.56 (m, 4H), 1.52–1.32 (m, 16H), 1.08–0.89 (m, 36H), 0.81–0.68 (m, 18H), 0.68–0.61 (m, 12H). <sup>13</sup>C NMR (101 MHz, CDCl<sub>3</sub>) δ 186.18, 165.65, 159.96, 159.50, 158.62, 155.51, 152.94, 152.81, 149.84, 149.63, 148.34, 138.88, 138.64, 138.30, 138.05, 136.50, 134.47, 123.87, 120.58, 118.89, 114.88, 114.72, 112.35, 112.15, 111.46, 69.99, 67.42, 53.89, 43.43, 35.53, 35.51, 34.26, 34.06, 31.89, 29.44, 29.36,

28.54, 28.49, 27.51, 27.31, 26.39, 22.80, 22.71, 14.14, 14.11, 14.07, 10.63. MS (MALDI-TOF): calcd for C<sub>98</sub>H<sub>114</sub>F<sub>4</sub>N<sub>4</sub>O<sub>4</sub>S<sub>4</sub> [M<sup>+</sup>] 1616.2476, found 1615.8367.

**Organic Solar Cell Fabrication and Measurement.** The inverted structure device of JS2:SMAs was fabricated with the device architecture of ITO/ZnO/PFN-Br/JS2:SMAs/MoOx/Ag. A thick layer of ZnO was deposited by spin-coating a ZnO precursor on top of pre-cleaned ITO substrates at 3000 rpm for 40 s, followed by annealing at 200 °C for 1 h in air. Subsequently, a thin layer of PFN-Br was spin-coated on ZnO for improving the interfacial properties. The substrates were then transferred into an argon-filled glovebox. Then, the blend solution of JS2:SMAs (6 mg mL<sup>-1</sup>, from CHCl<sub>3</sub> with 0.5% 1-chloronaphthalene, CN) was spin-coated at 1500 rpm for 20 s to form the active layer. After being thermally annealed at 120 °C for 10 min, the MoOx layer (6 nm) and the Ag layer (70 nm) were sequentially deposited by vacuum evaporation under 2 × 10<sup>-4</sup> Pa. The current density–voltage (*J*–*V*) curves of the fabricated devices were obtained by a Keithley 2400 source-measure unit. The photocurrent was measured under illumination with simulated 100 mW cm<sup>-2</sup> AM 1.5G irradiation using a SAN-EI XES-70S1 AAA class solar simulator, calibrated with a reference Si solar cell. The EQE spectrum was measured using a QE-R Solar Cell Spectral Response Measurement System (Enli Technology Co., Ltd., Taiwan).

## ASSOCIATED CONTENT

### Supporting Information

The Supporting Information is available free of charge at <https://pubs.acs.org/doi/10.1021/acs.chemmater.0c00097>.

Experimental details, synthesis route, density functional theory (DFT) calculations, GIWAXS patterns; synthesis route of SMAs (Figure S1); optimized molecular geometries and theoretical density distribution for the Frontier molecular orbitals of UF-C8-2F, UF-EH-2F, and UF-C2C5-2F (Figure S2); calculation data of UF-C8-2F, UF-EH-2F, and UF-C2C5-2F (Table S1); photovoltaic performances based on JS2:UF-Me-2F devices with different fabrication processes (Table S2) (PDF)

## AUTHOR INFORMATION

### Corresponding Author

**Yongsheng Chen** – The Key Laboratory of Functional Polymer Materials, State Key Laboratory and Institute of Elemento-Organic Chemistry, Centre of Nanoscale Science and Technology, College of Chemistry, Nankai University, Tianjin 300071, China; [orcid.org/0000-0003-1448-8177](https://orcid.org/0000-0003-1448-8177); Email: [yschen99@nankai.edu.cn](mailto:yschen99@nankai.edu.cn)

### Authors

**Meijia Chang** – The Key Laboratory of Functional Polymer Materials, State Key Laboratory and Institute of Elemento-Organic Chemistry, Centre of Nanoscale Science and Technology, College of Chemistry, Nankai University, Tianjin 300071, China; School of Environmental Engineering and Chemistry, Luoyang Institute of Science and Technology, Luoyang 471023, China

**Lingxian Meng** – The Key Laboratory of Functional Polymer Materials, State Key Laboratory and Institute of Elemento-Organic Chemistry, Centre of Nanoscale Science and Technology, College of Chemistry, Nankai University, Tianjin 300071, China

**Yunchuang Wang** – The Key Laboratory of Functional Polymer Materials, State Key Laboratory and Institute of Elemento-Organic Chemistry, Centre of Nanoscale Science and

Technology, College of Chemistry, Nankai University, Tianjin 300071, China

**Xin Ke** – The Key Laboratory of Functional Polymer Materials, State Key Laboratory and Institute of Elemento-Organic Chemistry, Centre of Nanoscale Science and Technology, College of Chemistry, Nankai University, Tianjin 300071, China

**Yuan-Qiu-Qiang Yi** – The Key Laboratory of Functional Polymer Materials, State Key Laboratory and Institute of Elemento-Organic Chemistry, Centre of Nanoscale Science and Technology, College of Chemistry, Nankai University, Tianjin 300071, China; [orcid.org/0000-0003-3522-7056](https://orcid.org/0000-0003-3522-7056)

**Nan Zheng** – Institute of Polymer Optoelectronic Materials and Devices, State Key Laboratory of Luminescent Materials and Devices, South China University of Technology, Guangzhou 510640, China

**Wenyu Zheng** – CAS Key Laboratory of Organic Solids, CAS Research/Education Center for Excellence in Molecular Sciences, Institute of Chemistry, Chinese Academy of Sciences, Beijing 100190, China

**Zengqi Xie** – Institute of Polymer Optoelectronic Materials and Devices, State Key Laboratory of Luminescent Materials and Devices, South China University of Technology, Guangzhou 510640, China; [orcid.org/0000-0002-9805-8176](https://orcid.org/0000-0002-9805-8176)

**Mingtao Zhang** – The Key Laboratory of Functional Polymer Materials, State Key Laboratory and Institute of Elemento-Organic Chemistry, Centre of Nanoscale Science and Technology, College of Chemistry, Nankai University, Tianjin 300071, China

**Yuanping Yi** – CAS Key Laboratory of Organic Solids, CAS Research/Education Center for Excellence in Molecular Sciences, Institute of Chemistry, Chinese Academy of Sciences, Beijing 100190, China; [orcid.org/0000-0002-0052-9364](https://orcid.org/0000-0002-0052-9364)

**Hongtao Zhang** – The Key Laboratory of Functional Polymer Materials, State Key Laboratory and Institute of Elemento-Organic Chemistry, Centre of Nanoscale Science and Technology, College of Chemistry, Nankai University, Tianjin 300071, China

**Xiangjian Wan** – The Key Laboratory of Functional Polymer Materials, State Key Laboratory and Institute of Elemento-Organic Chemistry, Centre of Nanoscale Science and Technology, College of Chemistry, Nankai University, Tianjin 300071, China

**Chenxi Li** – The Key Laboratory of Functional Polymer Materials, State Key Laboratory and Institute of Elemento-Organic Chemistry, Centre of Nanoscale Science and Technology, College of Chemistry, Nankai University, Tianjin 300071, China

Complete contact information is available at:

<https://pubs.acs.org/10.1021/acs.chemmater.0c00097>

### Author Contributions

<sup>†</sup>M.C. and L.M. contributed equally to this work.

### Notes

The authors declare no competing financial interest.

### ACKNOWLEDGMENTS

The authors gratefully acknowledge the financial support from MoST (2016YFA0200200, 2019YFA0705900), NSFC (21935007, 51773095, and 51873089), of China, Tianjin city (17JCJQC44500, 17JCZDJC31100), and 111 Project (B12015).

### REFERENCES

- (1) Li, N.; McCulloch, I.; Brabec, C. J. Analyzing the efficiency, stability and cost potential for fullerene-free organic photovoltaics in one figure of merit. *Energy Environ. Sci.* **2018**, *11*, 1355–1361.
- (2) Meng, L.; Zhang, Y.; Wan, X.; Li, C.; Zhang, X.; Wang, Y.; Ke, X.; Xiao, Z.; Ding, L.; Xia, R.; Yip, H. L.; Cao, Y.; Chen, Y. Organic and solution-processed tandem solar cells with 17.3% efficiency. *Science* **2018**, *361*, 1094–1098.
- (3) Yuan, J.; Zhang, Y.; Zhou, L.; Zhang, G.; Yip, H.-L.; Lau, T.-K.; Lu, X.; Zhu, C.; Peng, H.; Johnson, P. A.; Leclerc, M.; Cao, Y.; Ulanski, J.; Li, Y.; Zou, Y. Single-Junction Organic Solar Cell with over 15% Efficiency Using Fused-Ring Acceptor with Electron-Deficient Core. *Joule* **2019**, *3*, 1140–1151.
- (4) Fan, B.; Zhang, D.; Li, M.; Zhong, W.; Zeng, Z.; Ying, L.; Huang, F.; Cao, Y. Achieving over 16% efficiency for single-junction organic solar cells. *Sci. China Chem.* **2019**, *62*, 746–752.
- (5) An, Q.; Ma, X.; Gao, J.; Zhang, F. Solvent additive-free ternary polymer solar cells with 16.27% efficiency. *Sci. Bull.* **2019**, *64*, 504–506.
- (6) Baran, D.; Ashraf, R. S.; Hanifi, D. A.; Abdelsamie, M.; Gasparini, N.; Rohr, J. A.; Holliday, S.; Wadsworth, A.; Lockett, S.; Neophytou, M.; Emmott, C. J.; Nelson, J.; Brabec, C. J.; Amassian, A.; Salleo, A.; Kirchartz, T.; Durrant, J. R.; McCulloch, I. Reducing the efficiency-stability-cost gap of organic photovoltaics with highly efficient and stable small molecule acceptor ternary solar cells. *Nat. Mater.* **2017**, *16*, 363–369.
- (7) Du, X.; Heumueller, T.; Gruber, W.; Classen, A.; Unruh, T.; Li, N.; Brabec, C. J. Efficient Polymer Solar Cells Based on Non-fullerene Acceptors with Potential Device Lifetime Approaching 10 Years. *Joule* **2019**, *3*, 215–226.
- (8) Savagatrup, S.; Printz, A. D.; O'Connor, T. F.; Zaretski, A. V.; Rodriquez, D.; Sawyer, E. J.; Rajan, K. M.; Acosta, R. I.; Root, S. E.; Lipomi, D. J. Mechanical degradation and stability of organic solar cells: molecular and microstructural determinants. *Energy Environ. Sci.* **2015**, *8*, 55–80.
- (9) Cheng, P.; Zhan, X. Stability of organic solar cells: challenges and strategies. *Chem. Soc. Rev.* **2016**, *45*, 2544–2582.
- (10) Liu, X.; Zhang, C.; Duan, C.; Li, M.; Hu, Z.; Wang, J.; Liu, F.; Li, N.; Brabec, C. J.; Janssen, R. A. J.; Bazan, G. C.; Huang, F.; Cao, Y. Morphology Optimization via Side Chain Engineering Enables All-Polymer Solar Cells with Excellent Fill Factor and Stability. *J. Am. Chem. Soc.* **2018**, *140*, 8934–8943.
- (11) Fan, B. B.; Du, X. Y.; Liu, F.; Zhong, W. K.; Ying, L.; Xie, R. H.; Tang, X. F.; An, K.; Xin, J. M.; Li, N.; Ma, W.; Brabec, C. J.; Huang, F.; Cao, Y. Fine-tuning of the chemical structure of photoactive materials for highly efficient organic photovoltaics. *Nat. Energy* **2018**, *3*, 1051–1058.
- (12) Yang, Y.; Zhang, Z. G.; Bin, H.; Chen, S.; Gao, L.; Xue, L.; Yang, C.; Li, Y. Side-Chain Isomerization on an n-type Organic Semiconductor ITIC Acceptor Makes 11.77% High Efficiency Polymer Solar Cells. *J. Am. Chem. Soc.* **2016**, *138*, 15011–15018.
- (13) Li, Y.; Zheng, N.; Yu, L.; Wen, S.; Gao, C.; Sun, M.; Yang, R. A Simple Phenyl Group Introduced at the Tail of Alkyl Side Chains of Small Molecular Acceptors: New Strategy to Balance the Crystallinity of Acceptors and Miscibility of Bulk Heterojunction Enabling Highly Efficient Organic Solar Cells. *Adv. Mater.* **2019**, *31*, No. 1807832.
- (14) Feng, H. R.; Qiu, N. L.; Wang, X.; Wang, Y. C.; Kan, B.; Wan, X. J.; Zhang, M. T.; Xia, A. D.; Li, C. X.; Liu, F.; Zhang, H. T.; Chen, Y. S. An A-D-A Type Small-Molecule Electron Acceptor with End-Extended Conjugation for High Performance Organic Solar Cells. *Chem. Mater.* **2017**, *29*, 7908–7917.
- (15) Zhao, Q.; Yu, X.; Xie, Z.; Liu, J.; Han, Y. Optimizing H-/J-Type Aggregation and Vertical Phase Separation to Improve Photovoltaic Efficiency of Small Molecule Solar Cells by Adding a Macromolecule Additive. *ACS Appl. Energy Mater.* **2018**, *1*, 6338–6344.
- (16) Wu, Y.; Yang, H.; Zou, Y.; Dong, Y. Y.; Yuan, J. Y.; Cui, C. H.; Li, Y. F. A new dialkylthio-substituted naphtho[2,3-c]thiophene-4,9-dione based polymer donor for high-performance polymer solar cells. *Energy Environ. Sci.* **2019**, *12*, 675–683.

- (17) Chen, L. X. Beyond PCE: Looking at a Big Picture in Photovoltaic Research. *ACS Energy Lett.* **2018**, *3*, 1967–1968.
- (18) Jørgensen, M.; Norrman, K.; Gevorgyan, S. A.; Tromholt, T.; Andreasen, B.; Krebs, F. C. Stability of polymer solar cells. *Adv. Mater.* **2012**, *24*, 580–612.
- (19) Mateker, W. R.; McGehee, M. D. Progress in Understanding Degradation Mechanisms and Improving Stability in Organic Photovoltaics. *Adv. Mater.* **2017**, *29*, No. 1603940.
- (20) Gasparini, N.; Salvador, M.; Strohm, S.; Heumueller, T.; Levchuk, I.; Wadsworth, A.; Bannock, J. H.; de Mello, J. C.; Egelhaaf, H. J.; Baran, D.; McCulloch, I.; Brabec, C. J. Burn-in Free Nonfullerene-Based Organic Solar Cells. *Adv. Energy Mater.* **2017**, *7*, No. 1700770.
- (21) Cha, H.; Wu, J.; Wadsworth, A.; Nagitta, J.; Limbu, S.; Pont, S.; Li, Z.; Searle, J.; Wyatt, M. F.; Baran, D.; Kim, J. S.; McCulloch, I.; Durrant, J. R. An Efficient, “Burn in” Free Organic Solar Cell Employing a Nonfullerene Electron Acceptor. *Adv. Mater.* **2017**, *29*, No. 1701156.
- (22) Wang, Y.; Lan, W.; Li, N.; Lan, Z.; Li, Z.; Jia, J.; Zhu, F. Stability of Nonfullerene Organic Solar Cells: from Built-in Potential and Interfacial Passivation Perspectives. *Adv. Energy Mater.* **2019**, *9*, No. 1900157.
- (23) Zhang, C.; Heumueller, T.; Gruber, W.; Almora, O.; Du, X.; Ying, L.; Chen, J.; Unruh, T.; Cao, Y.; Li, N.; Brabec, C. J. Comprehensive Investigation and Analysis of Bulk-Heterojunction Microstructure of High-Performance PCE11:PCBM Solar Cells. *ACS Appl. Mater. Interfaces* **2019**, *11*, 18555–18563.
- (24) Zhang, C.; Heumueller, T.; Leon, S.; Gruber, W.; Burlafinger, K.; Tang, X.; Perea, J. D.; Wabra, I.; Hirsch, A.; Unruh, T.; Li, N.; Brabec, C. J. A top-down strategy identifying molecular phase stabilizers to overcome microstructure instabilities in organic solar cells. *Energy Environ. Sci.* **2019**, *12*, 1078–1087.
- (25) Guerrero, A.; Garcia-Belmonte, G. Recent Advances to Understand Morphology Stability of Organic Photovoltaics. *Nano-Micro Lett.* **2017**, *9*, 10.
- (26) Liu, Y.; Zhao, J.; Li, Z.; Mu, C.; Ma, W.; Hu, H.; Jiang, K.; Lin, H.; Ade, H.; Yan, H. Aggregation and morphology control enables multiple cases of high-efficiency polymer solar cells. *Nat. Commun.* **2014**, *5*, No. 5293.
- (27) Ghasemi, M.; Hu, H.; Peng, Z.; Rech, J. J.; Angunawela, I.; Carpenter, J. H.; Stuard, S. J.; Wadsworth, A.; McCulloch, I.; You, W.; Ade, H. Delineation of Thermodynamic and Kinetic Factors that Control Stability in Non-fullerene Organic Solar Cells. *Joule* **2019**, *3*, 1328–1348.
- (28) Cheng, P.; Yan, C.; Lau, T. K.; Mai, J.; Lu, X.; Zhan, X. Molecular Lock: A Versatile Key to Enhance Efficiency and Stability of Organic Solar Cells. *Adv. Mater.* **2016**, *28*, 5822–5829.
- (29) Zhou, K.; Xin, J. M.; Ma, W. Hierarchical Morphology Stability under Multiple Stresses in Organic Solar Cells. *ACS Energy Lett.* **2019**, *4*, 447–455.
- (30) Li, N.; Perea, J. D.; Kassar, T.; Richter, M.; Heumueller, T.; Matt, G. J.; Hou, Y.; Guldal, N. S.; Chen, H.; Chen, S.; Langner, S.; Berlinghof, M.; Unruh, T.; Brabec, C. J. Abnormal strong burn-in degradation of highly efficient polymer solar cells caused by spinodal donor-acceptor demixing. *Nat. Commun.* **2017**, *8*, No. 14541.
- (31) Zhang, G.; Zhao, J.; Chow, P. C. Y.; Jiang, K.; Zhang, J.; Zhu, Z.; Zhang, J.; Huang, F.; Yan, H. Nonfullerene Acceptor Molecules for Bulk Heterojunction Organic Solar Cells. *Chem. Rev.* **2018**, *118*, 3447–3507.
- (32) Hou, J.; Inganas, O.; Friend, R. H.; Gao, F. Organic solar cells based on non-fullerene acceptors. *Nat. Mater.* **2018**, *17*, 119–128.
- (33) Cheng, P.; Li, G.; Zhan, X. W.; Yang, Y. Next-generation organic photovoltaics based on non-fullerene acceptors. *Nat. Photonics* **2018**, *12*, 131–142.
- (34) Shen, F. G.; Xu, J. Z.; Li, X. M.; Zhan, C. L. Nonfullerene small-molecule acceptors with perpendicular side-chains for fullerene-free solar cells. *J. Mater. Chem. A* **2018**, *6*, 15433–15455.
- (35) Zhang, H.; Yao, H.; Hou, J.; Zhu, J.; Zhang, J.; Li, W.; Yu, R.; Gao, B.; Zhang, S.; Hou, J. Over 14% Efficiency in Organic Solar Cells Enabled by Chlorinated Nonfullerene Small-Molecule Acceptors. *Adv. Mater.* **2018**, *30*, No. 1800613.
- (36) Kan, B.; Zhang, J.; Liu, F.; Wan, X.; Li, C.; Ke, X.; Wang, Y.; Feng, H.; Zhang, Y.; Long, G.; Friend, R. H.; Bakulin, A. A.; Chen, Y. Fine-Tuning the Energy Levels of a Nonfullerene Small-Molecule Acceptor to Achieve a High Short-Circuit Current and a Power Conversion Efficiency over 12% in Organic Solar Cells. *Adv. Mater.* **2018**, *30*, No. 1704904.
- (37) Dai, S.; Zhao, F.; Zhang, Q.; Lau, T. K.; Li, T.; Liu, K.; Ling, Q.; Wang, C.; Lu, X.; You, W.; Zhan, X. Fused Nonacyclic Electron Acceptors for Efficient Polymer Solar Cells. *J. Am. Chem. Soc.* **2017**, *139*, 1336–1343.
- (38) Luo, Z.; Liu, T.; Wang, Y.; Zhang, G.; Sun, R.; Chen, Z.; Zhong, C.; Wu, J.; Chen, Y.; Zhang, M.; Zou, Y.; Ma, W.; Yan, H.; Min, J.; Li, Y.; Yang, C. Reduced Energy Loss Enabled by a Chlorinated Thiophene-Fused Ending-Group Small Molecular Acceptor for Efficient Nonfullerene Organic Solar Cells with 13.6% Efficiency. *Adv. Energy Mater.* **2019**, *9*, No. 1900041.
- (39) Kan, B.; Feng, H. R.; Yao, H. F.; Chang, M. J.; Wan, X. J.; Li, C. X.; Hou, J. H.; Chen, Y. S. A chlorinated low-bandgap small-molecule acceptor for organic solar cells with 14.1% efficiency and low energy loss. *Sci. China Chem.* **2018**, *61*, 1307–1313.
- (40) Liu, Y.; Li, M.; Zhou, X.; Jia, Q.-Q.; Feng, S.; Jiang, P.; Xu, X.; Ma, W.; Li, H.-B.; Bo, Z. Nonfullerene Acceptors with Enhanced Solubility and Ordered Packing for High-Efficiency Polymer Solar Cells. *ACS Energy Lett.* **2018**, *3*, 1832–1839.
- (41) Zhang, C.; Feng, S.; Liu, Y.; Hou, R.; Zhang, Z.; Xu, X.; Wu, Y.; Bo, Z. Effect of Non-fullerene Acceptors’ Side Chains on the Morphology and Photovoltaic Performance of Organic Solar Cells. *ACS Appl. Mater. Interfaces* **2017**, *9*, 33906–33912.
- (42) Chang, M. J.; Wang, Y. C.; Yi, Y. Q.; Ke, X.; Wan, X. J.; Li, C. X.; Chen, Y. S. Fine-tuning the side-chains of non-fullerene small molecule acceptors to match with appropriate polymer donors. *J. Mater. Chem. A* **2018**, *6*, 8586–8594.
- (43) Lee, H.; Park, C.; Sin, D. H.; Park, J. H.; Cho, K. Recent Advances in Morphology Optimization for Organic Photovoltaics. *Adv. Mater.* **2018**, *30*, No. 1800453.
- (44) Li, S.; Zhan, L.; Liu, F.; Ren, J.; Shi, M.; Li, C. Z.; Russell, T. P.; Chen, H. An Unfused-Core-Based Nonfullerene Acceptor Enables High-Efficiency Organic Solar Cells with Excellent Morphological Stability at High Temperatures. *Adv. Mater.* **2018**, *30*, No. 1705208.
- (45) Li, S.; Zhan, L.; Sun, C.; Zhu, H.; Zhou, G.; Yang, W.; Shi, M.; Li, C. Z.; Hou, J.; Li, Y.; Chen, H. Highly Efficient Fullerene-Free Organic Solar Cells Operate at Near Zero Highest Occupied Molecular Orbital Offsets. *J. Am. Chem. Soc.* **2019**, *141*, 3073–3082.
- (46) Yu, Z. P.; Liu, Z. X.; Chen, F. X.; Qin, R.; Lau, T. K.; Yin, J. L.; Kong, X.; Lu, X.; Shi, M.; Li, C. Z.; Chen, H. Simple non-fused electron acceptors for efficient and stable organic solar cells. *Nat. Commun.* **2019**, *10*, No. 2152.
- (47) Huang, H.; Guo, Q.; Feng, S.; Zhang, C.; Bi, Z.; Xue, W.; Yang, J.; Song, J.; Li, C.; Xu, X.; Tang, Z.; Ma, W.; Bo, Z. Noncovalently fused-ring electron acceptors with near-infrared absorption for high-performance organic solar cells. *Nat. Commun.* **2019**, *10*, No. 3038.
- (48) Xue, R.; Zhang, J.; Li, Y.; Li, Y. Organic Solar Cell Materials toward Commercialization. *Small* **2018**, *14*, No. 1801793.
- (49) Zhang, J.; Tan, H. S.; Guo, X.; Facchetti, A.; Yan, H. Material insights and challenges for non-fullerene organic solar cells based on small molecular acceptors. *Nat. Energy* **2018**, *3*, 720–731.
- (50) Zhan, L.; Li, S.; Zhang, S.; Chen, X.; Lau, T. K.; Lu, X.; Shi, M.; Li, C. Z.; Chen, H. Enhanced Charge Transfer between Fullerene and Non-Fullerene Acceptors Enables Highly Efficient Ternary Organic Solar Cells. *ACS Appl. Mater. Interfaces* **2018**, *10*, 42444–42452.
- (51) Feng, H.; Yi, Y. Q.; Ke, X.; Yan, J.; Zhang, Y.; Wan, X.; Li, C.; Zheng, N.; Xie, Z.; Chen, Y. New Anthracene-Fused Nonfullerene Acceptors for High-Efficiency Organic Solar Cells: Energy Level Modulations Enabling Match of Donor and Acceptor. *Adv. Energy Mater.* **2019**, *9*, No. 1803541.
- (52) Kim, K.-H.; Kang, H.; Kim, H. J.; Kim, P. S.; Yoon, S. C.; Kim, B. J. Effects of Solubilizing Group Modification in Fullerene Bis-

Adducts on Normal and Inverted Type Polymer Solar Cells. *Chem. Mater.* **2012**, *24*, 2373–2381.

(53) Nilsson, S.; Bernasik, A.; Budkowski, A.; Moons, E. Morphology and Phase Segregation of Spin-Casted Films of Polyfluorene/PCBM Blends. *Macromolecules* **2007**, *40*, 8291–8301.

(54) Liu, W.; Zhang, J.; Zhou, Z.; Zhang, D.; Zhang, Y.; Xu, S.; Zhu, X. Design of a New Fused-Ring Electron Acceptor with Excellent Compatibility to Wide-Bandgap Polymer Donors for High-Performance Organic Photovoltaics. *Adv. Mater.* **2018**, *30*, No. 1800403.

(55) Toolan, D. T.; Pullan, N.; Harvey, M. J.; Topham, P. D.; Howse, J. R. In situ studies of phase separation and crystallization directed by Marangoni instabilities during spin-coating. *Adv. Mater.* **2013**, *25*, 7033–7037.

(56) Xin, J.; Meng, X.; Xu, X.; Zhu, Q.; Naveed, H. B.; Ma, W. Cold Crystallization Temperature Correlated Phase Separation, Performance, and Stability of Polymer Solar Cells. *Matter* **2019**, *1*, 1316–1330.